

The structural properties of InGaN alloys and the interdependence on the thermoelectric behavior

Cite as: AIP Advances 6, 025305 (2016); <https://doi.org/10.1063/1.4941934>

Submitted: 25 November 2015 • Accepted: 27 January 2016 • Published Online: 09 February 2016

Bahadir Kucukgok,  Xuewang Wu, Xiaojia Wang, et al.



View Online



Export Citation



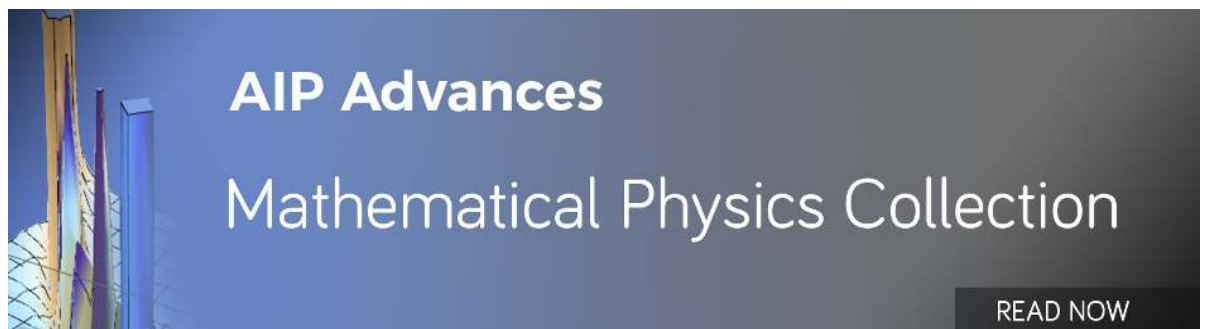
CrossMark

ARTICLES YOU MAY BE INTERESTED IN

[Electronic band structures and effective-mass parameters of wurtzite GaN and InN](#)
Journal of Applied Physics **83**, 1429 (1998); <https://doi.org/10.1063/1.366847>

[High temperature thermoelectric properties of optimized InGaN](#)
Journal of Applied Physics **110**, 123709 (2011); <https://doi.org/10.1063/1.3670966>

[Thermoelectric properties of In-rich InGaN and InN/InGaN superlattices](#)
AIP Advances **6**, 045216 (2016); <https://doi.org/10.1063/1.4948446>



AIP Advances
Mathematical Physics Collection

READ NOW

The structural properties of InGaN alloys and the interdependence on the thermoelectric behavior

Bahadır Kucukgok,¹ Xuewang Wu,² Xiaojia Wang,² Zhiqiang Liu,³
 Ian T. Ferguson,⁴ and Na Lu^{1,a}

¹Lyles School of Civil Engineering, Purdue University, West Lafayette, IN 47907, USA

²Department of Mechanical Engineering, University of Minnesota, Minneapolis, MN 55455, USA

³Institute of Semiconductors, Chinese Academy of Science, Beijing, China

⁴College of Engineering and Computing, Missouri University of Science and Technology, Rolla, MO 65409, USA

(Received 25 November 2015; accepted 27 January 2016; published online 9 February 2016)

The III-Nitrides are promising candidate for high efficiency thermoelectric (TE) materials and devices due to their unique features which includes high thermal stability. A systematic study of the room temperature TE properties of metalorganic chemical vapor deposition grown $\text{In}_x\text{Ga}_{1-x}\text{N}$ were investigated for $x=0.07$ to 0.24 . This paper investigated the role of indium composition on the TE properties of InGaN alloys in particular the structural properties for homogenous material that did not show significant phase separation. The highest Seebeck and power factor values of $507 \mu\text{VK}^{-1}$ and $21.84 \times 10^{-4} \text{ Wm}^{-1}\text{K}^{-1}$ were observed, respectively for $\text{In}_{0.07}\text{Ga}_{0.93}\text{N}$ at room temperature. The highest value of figure-of-merit (ZT) was calculated to be 0.072 for $\text{In}_{0.20}\text{Ga}_{0.80}\text{N}$ alloy at room temperature. © 2016 Author(s). All article content, except where otherwise noted, is licensed under a Creative Commons Attribution (CC BY) license (<http://creativecommons.org/licenses/by/4.0/>). [<http://dx.doi.org/10.1063/1.4941934>]

Thermoelectric (TE) devices have attracted tremendous interest as a renewable energy source, due to their ability to convert waste heat to electricity (Seebeck effect).^{1,2} The efficiency of a TE material is determined by the figure-of-merit $ZT=S^2\sigma T/\kappa$ where S is the Seebeck coefficient, σ is the electrical conductivity, T is the absolute temperature, and κ is the thermal conductivity. Thermal conductivity consists of two contributions, namely, the lattice thermal conductivity (κ_l) and the electronic part (κ_e).³⁻⁶ It is very difficult to obtain high ZT value in a single material system because all properties are interdependent. For instance, higher carrier concentration often lead to higher electrical conductivity, but result in low Seebeck coefficient and high thermal conductivity due to increased electronic contribution due to the Wiedemann-Franz law.^{7,2,1} Ioffe *et al.*⁸ calculated that the optimum charge carrier's density that is good for TE materials needs to be in the range of 10^{18} - 10^{19} cm^{-3} . Therefore, the best reported TE materials are often degenerately doped semiconductors, such as Bi_2Te_3 - Sb_2Te_3 , PbTe and $\text{Si}_{1-x}\text{Ge}_x$ and ZTs of ~ 1 are often reported at room temperature. However, the use of TE devices fabricated using these materials are limited due to their toxicity (Te elements), high cost (SiGe), and a poor stability at high temperatures.⁹ Therefore, recent research efforts have mostly focused on developing new TE materials, which are non-toxic and have superior thermal stability at high temperature ranges.¹⁰

The interest of utilizing III-Nitrides semiconductors such as GaN, InGaN, InAlN, and AlGaIn in the TE applications is increasing due to their promising ZT values at a wide range temperatures, 300-1300 K, that cannot be accessed by other materials.¹¹ For instance, a ZT value of 0.08 at room temperature and 0.23 at 450 K for $\text{In}_{0.36}\text{Ga}_{0.64}\text{N}$ has been reported.¹² Furthermore, a rapid increase of ZT value with temperature was observed in $\text{In}_{0.17}\text{Ga}_{0.83}\text{N}$, reaching a maximum ZT of 0.34 at

^aElectronic mail: Luna@purdue.edu

875 K.¹³ More recently, ZT value of 0.08 was also obtained at room temperature using polarization field engineering of GaN/AlN/AlGaN superlattices.¹⁴ In addition, theoretical studies have also been conducted on TE properties of bulk GaN, AlGaN and InGaN alloys using electron-transport models that consider various electron-scattering mechanisms.^{15–17}

Consequently, these initial experimental and theoretical studies indicate that III-Nitrides could have acceptable TE properties for power generation. However, the effect of structural quality of the III-Nitrides in particular the dislocation density on TE properties has not been fully investigated. Therefore, in this work, the correlation between structural and optical properties of InGaN alloys with various indium (In) compositions and the TE properties are investigated.

All the InGaN samples studied here were grown on c-plane sapphire substrate with 2 μm thick undoped GaN template using metal organic vapor deposition (MOCVD). The precursors for Ga, N, In, and Si were trimethylgallium (TMGa), ammonia (NH_3), trimethylindium (TMIn), and silane, respectively. Hydrogen and nitrogen were used as the carrier gases and silicon was used as n-type dopants with controlled carrier concentration ranging from 10^{17} - 10^{19} . Detailed information for the growth conditions for InGaN have been reported elsewhere.^{18,19}

The in-plane electrical conductivity, carrier density and electron mobility was obtained using Van der Pauw Hall-effect method. In-plane Seebeck coefficients of all samples were measured using standard temperature gradient technique, as reported in elsewhere.²⁴ The estimated uncertainty in Van der Pauw Hall and Seebeck measurements were approximately $\pm 5\%$. The film thickness was measured using both in-situ and ex-situ spectral reflectometry with ± 2 - 3% error. High resolution X-ray diffraction (HRXRD) triple-axis diffractometer was employed on all of the samples for structural characterization. A room temperature deep ultraviolet (DUV) photoluminescence (PL) spectroscopy (excitation at 248 nm) was used to measure the optical properties of the material.

The through-plane thermal conductivities of all samples were measured using time-domain thermoreflectance (TDTR).^{17,20} It is reasonable to assume that the thermal transport is isotropic for all samples due to the homogenous nature of InGaN at lower alloy compositions. The samples were coated with thin films of aluminum (Al) to serve as metal transducers. For each sample, a $5\times$ objective lens with a beam spot of 12 μm were used. The thermal conductivity of the Al transducer was obtained from the Wiedemann Franz Law together with four-point probe electrical measurements. The thickness of the Al transducer was determined from picosecond acoustics.²⁰ The return time and shape of the acoustic echoes depend on the layer thicknesses and acoustic impedances ($Z=\rho v$ with ρ being the mass density and v being speed of sound, respectively). For acoustically soft Al transducer on acoustically stiffer InGaN ($Z_{\text{Al}} < Z_{\text{InGaN}}$), the first echo is upward followed by a downward second echo.²¹ However, Figure 1(a) exhibits different features: the first acoustic echo is approximately anti-symmetric with a negative peak followed by a positive peak, and the second echo has a positive peak. These unusual features imply that there exists a soft contamination layer in between the Al transducer layer and the InGaN thin film. Following heuristics proposed by Hohensee *et al.*,²¹ the inflection point (the “zero-crossing” point with respect to the thermal background) was chosen, as the return time of the first acoustic echo. This results in a thickness ≈ 83 nm for the Al transducer. The thermal conductivities of all four samples were extracted by fitting the TDTR signal to a thermal model,²² as illustrated by the excellent agreement between the model calculation (red solid lines) and the measurement data (symbols) in Figure 1(b). The penetration depth of thermal waves modulated at 18 MHz or 9 MHz is longer than the film thickness; therefore the InGaN/GaN interface will affect the fitting of InGaN thermal conductivity. The interfacial thermal conductance of InGaN/GaN has not been reported; therefore a value for the epitaxial AlN/GaN interface ($600 \text{ Wm}^{-2}\text{K}^{-1}$) was used for thermal modeling.²³ This value was assumed to be reasonable considering that the epitaxial growth in MOCVD typically produces good interfaces which shall possess large thermal conductances.

Indium compositions of all InGaN alloys were analyzed using XRD. The c lattice parameter of the $\text{In}_x\text{Ga}_{1-x}\text{N}$ films was evaluated directly from the symmetric (0002) reflection.^{24–26} However, due to the high lattice mismatch the role of strain also needed to be considered. As InGaN epilayers on GaN are fully strained when the total film thickness is less than a critical thickness.^{24,25,27}

Figure 2 shows HRXRD 2θ - ω scan data of the (0002) reflections for InGaN alloys. All samples depict sharp peak (002) from the thick GaN template layer and the broader peak at a lower angle

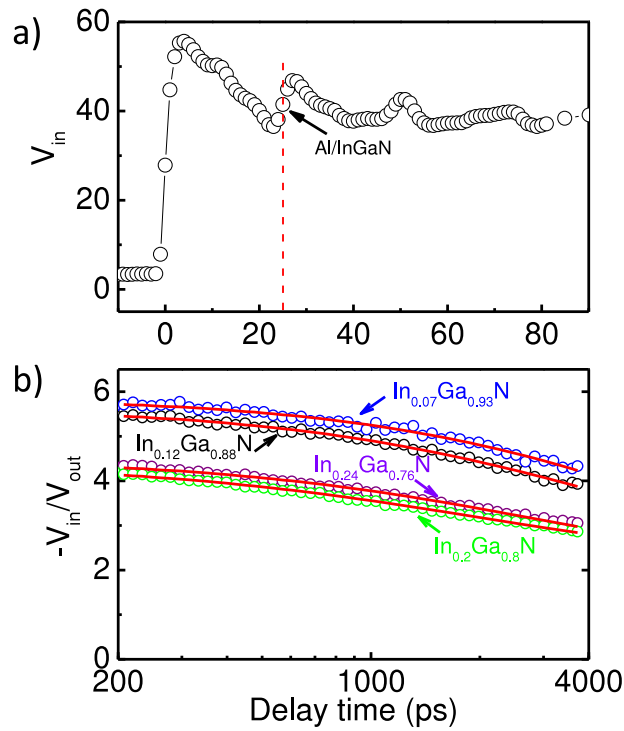


FIG. 1. (a) Representative picosecond acoustics of sample $\text{In}_{0.12}\text{Ga}_{0.88}\text{N}$ at short time delay for determining the thickness of the Al transducer and (b) TDTR data (symbols) and thermal modeling (red solid lines) of all four samples.

(002) from the InGaN. The broadened XRD peaks could be attributed to inhomogeneous strain induced by deformations and stresses incorporated at the substrate and epilayers.^{17,28} Additionally, edge and screw dislocations in III-Nitrides often lead to broadening of X-ray reflection as shown in this study. To further understand the effect of dislocation density on TE property of materials, the

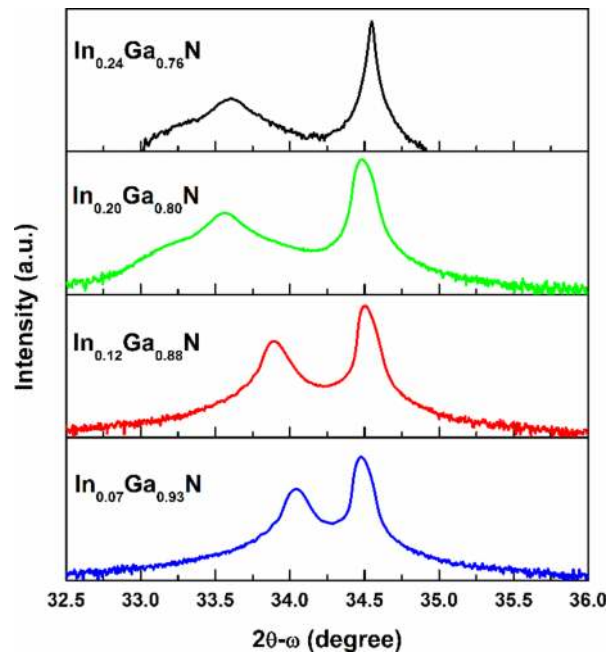


FIG. 2. XRD spectra of $2\theta-\omega$ scan on symmetric (0002) reflections of the each sample with respect to indium compositions. The sharp distinct peaks correspond to the template GaN layer and the five peaks on the left represent the InGaN epilayers.

density of threading screw and mixed dislocations were calculated.²⁹ The average dislocation densities (TDs) in $\text{In}_x\text{Ga}_{1-x}\text{N}$ were calculated as 5.75×10^7 , 8.50×10^7 , 8.30×10^8 , and $2.68 \times 10^9 \text{ cm}^{-2}$ for $x = 0.07, 0.12, 0.20,$ and 0.24 . Additionally, the full width half maximum (FWHM) and thickness values of each sample increased 237, 288, 900, 1620 arcsec and 114, 120, 125, 145nm, respectively with increasing indium composition. TDs result indicates that increasing indium composition degrades the crystal quality of InGaN alloys. It is important to point out that TDs of InGaN alloys increased one order of magnitude when the indium composition reaches $\sim 20\%$, and this may be the composition threshold for achieving high crystal InGaN alloys. Furthermore, no significant evidence of phase separation was observed up to these indium compositions. This was due to the growth regime used to grow these samples and is most likely due to the coherence strain which could stabilize the alloys against phase separation.^{30,31}

Room temperature PL spectra were also used to determine bandgaps of the $\text{In}_x\text{Ga}_{1-x}\text{N}$ samples, Figure 3. The band gap values shift to lower energy as indium composition increases with a corresponding increase in the emission linewidth. The broadening of the emission linewidth can be associated with defects related to indium and random alloy fluctuations. Additionally, PL peaks can also become broadened as thickness value increases due to the fact that enhanced role of deep levels regarding to band edge emission in the thick films.³² PL spectra also revealed the absence of InGaN phase separation.

Figure 4 illustrates the Seebeck coefficient, power factor, mobility, and electrical conductivity as a function of indium composition ranging from 0.07 to 0.24. The carrier densities of each InGaN alloy are also shown for comparison. All the other TE parameters decrease as the indium composition increases except the electrical conductivity. The Seebeck coefficient of $\text{In}_x\text{Ga}_{1-x}\text{N}$ was measured as $507 \mu\text{VK}^{-1}$, $440 \mu\text{VK}^{-1}$, $420 \mu\text{VK}^{-1}$, and $280 \mu\text{VK}^{-1}$ for $x = 0.07, 0.12, 0.20,$ and 0.24 . All the InGaN samples in this study showed negative Seebeck coefficients which indicated that they are n-type materials consistent with them being Si-doped. Furthermore, the reduction trend in Seebeck coefficient can be attributed to the lower electron effective mass of InN ($0.11m_e$) compared to that of GaN ($0.20m_e$). As indium composition increases, the electron effective mass of InGaN alloys reduce resulting in lower Seebeck coefficient value. Additionally, as indium replaces Ga, the band gap of alloys also decreases (Figure 3) which results in lower Seebeck coefficient.

The highest power factor of $\text{In}_x\text{Ga}_{1-x}\text{N}$ alloys is $21.84 \times 10^{-4} \text{ Wm}^{-1}\text{K}^{-1}$ at $x = 0.07$. The reduction in power factor with the increase of indium composition is observed due to the sharply reduced

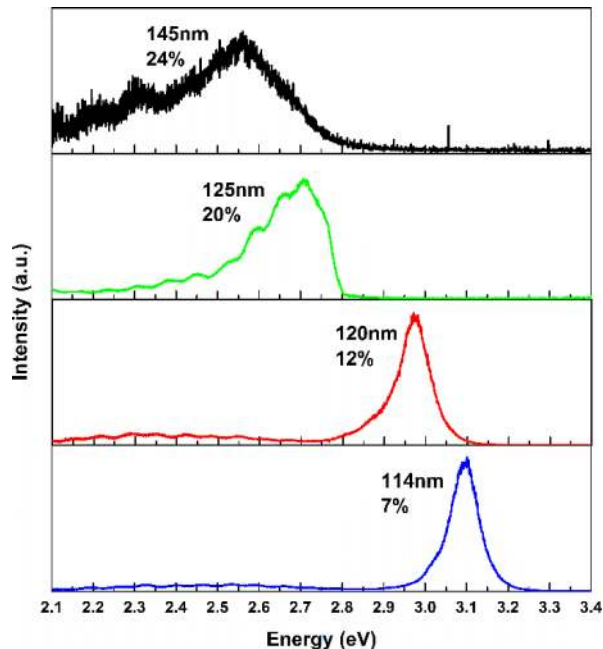


FIG. 3. Band gap of $\text{In}_x\text{Ga}_{1-x}\text{N}$ epitaxial films obtained from DUV PL at room temperature.

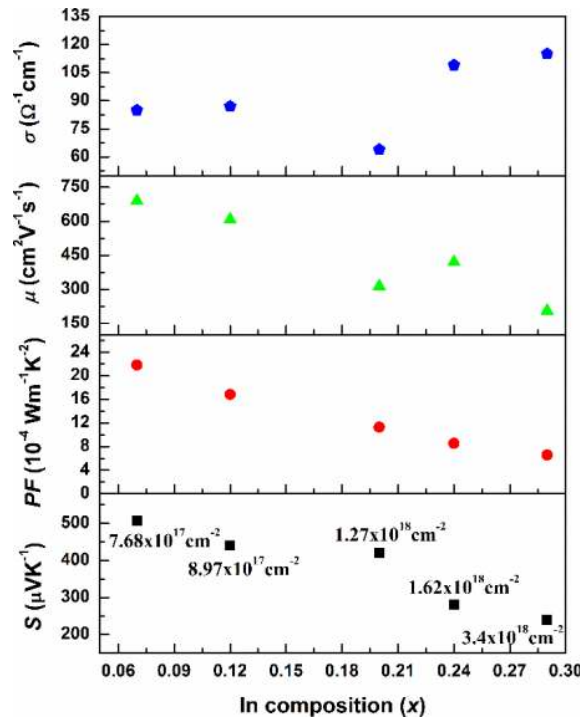


FIG. 4. Room temperature electrical conductivity (σ), electron mobility (μ), power factor ($S^2\sigma$), and Seebeck coefficient (S) of InGaN as a function of indium composition (x). Carrier densities are also shown to make comparison.

Seebeck coefficient. As it can be observed from Figure 2 $\text{In}_{0.20}\text{Ga}_{0.80}\text{N}$ shows very broad peak FWHM of 900 arcsec due to its degraded crystal quality induced by impurities and extended defects, such as screw and mixed dislocations and result in high TD of $8.30 \times 10^8 \text{ cm}^{-2}$. Consequently, these defects form scattering centers in the electrons' path and resulting in a rapid drop in mobility. Power factor also shows exponential decay in respect to carrier density due to the dominant effect of Seebeck coefficient via its formula $S^2\sigma$ although electrical conductivity increases.

The reduction in mobility of InGaN alloy can be attributed to enhanced alloy scattering effect with increase in indium composition. Alloying the material leads to more electrons scattering due to the dissimilar electrical properties between In and Ga.¹³ Additionally, a rapid drop of mobility of $\text{In}_x\text{Ga}_{1-x}\text{N}$ is observed at $x=0.20$ due to the high dislocation scattering of electrons, that is, the dislocation density increased from $5.75 \times 10^7 \text{ cm}^{-2}$ for $x=0.07$ to $8.30 \times 10^8 \text{ cm}^{-2}$ for $x=0.20$. Moreover, electrical conductivity typically decreases while indium composition increases, however opposite behavior was observed. This can be associated with increased electrically active crystal defects, which can act as donors. It is important to point that the background carrier density of $\text{In}_x\text{Ga}_{1-x}\text{N}$ has increased from $7.68 \times 10^{17} \text{ cm}^{-3}$ to $1.62 \times 10^{18} \text{ cm}^{-3}$ for $x=0.07$ to $x=0.24$. This increased carrier density may dominant the electron transport mechanism despite mobility reduction and thus result in electrical conductivity enhancement. The relationship between carrier density and indium composition is presented in Figure 4 and Table I.

TABLE I. Summary of all InGaN alloys investigated. The samples were grown by MOCVD on sapphire substrate with GaN buffer layers.

Seebeck (μVK^{-1})	Power Factor ($10^{-4}\text{Wm}^{-1}\text{K}^{-1}$)	Conductivity ($\Omega^{-1}\text{cm}^{-1}$)	Mobility ($\text{cm}^{-2}\text{V}^{-1}\text{s}^{-1}$)	Carrier Density (cm^{-3})	Thermal Conductivity ($\text{Wm}^{-1}\text{K}^{-1}$)	ZT	Indium Composition (x)
507	21.84	85	690	7.68×10^{17}	11 +/- 2.3	0.059	~7%
440	16.84	87	608	8.97×10^{17}	7.7 +/- 1.4	0.065	~12%
420	11.28	64	314	1.27×10^{18}	4.7 +/- 0.8	0.072	~20%
280	8.54	109	420	1.62×10^{18}	5.5 +/- 1.0	0.046	~24%

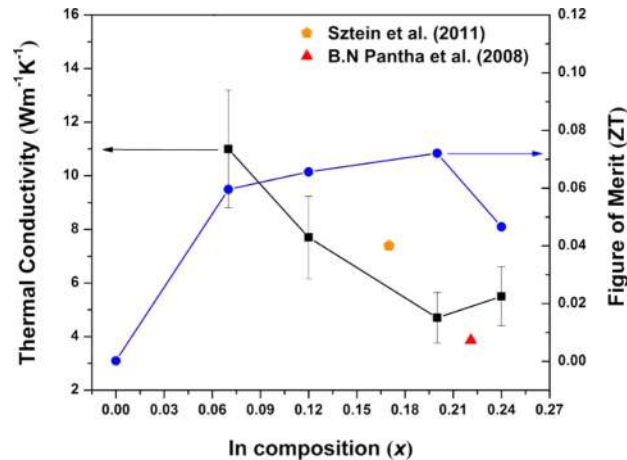


FIG. 5. Room temperature thermal conductivity (κ) and ZT for InGaN vs. indium composition. Thermal conductivity values are measured by TDTR from University of Minnesota. To calculate ZT at $x=0\%$, room temperature thermal conductivity value of thin film GaN is also shown (Ref. 33). ZTs for $\text{In}_{0.17}\text{Ga}_{0.83}\text{N}$ and $\text{In}_{0.22}\text{Ga}_{0.78}\text{N}$ from Ref. 13 and Ref. 12, respectively are included for comparison.

Figure 5 depicts thermal conductivities of $\text{In}_x\text{Ga}_{1-x}\text{N}$ alloys with $x=0.07-0.24$ at room temperature. As can be seen, thermal conductivity of alloys has drastically reduced from $11 \text{ Wm}^{-1}\text{K}^{-1}$ to $4.7 \text{ Wm}^{-1}\text{K}^{-1}$ from $x=0.07$ to $x=0.20$. The reduction in the thermal conductivity can also be attributed to alloy scattering mechanism. The ZT values for alloys at room temperature are also shown in Figure 5. The highest ZT value is observed as 0.072 for $\text{In}_{0.20}\text{Ga}_{0.80}\text{N}$, due to the lowest thermal conductivity of this sample. To calculate ZT value of InGaN alloy at $x=0$, room temperature Seebeck coefficient ($187\mu\text{VK}^{-1}$) and thermal conductivity values of thin film GaN ($\sim 50 \text{ Wm}^{-1}\text{K}^{-1}$)³³ are used. The variation of ZT value with indium composition is attributed to alloy scattering dominated transport and it should be mentioned that the measurement error in the thermal conductivity data (represented by error bars in Figure 5) was associated with surface roughness, film thickness, and high indium compositions. The primary reason for the reduction of the thermal conductivity as composition increases is because higher indium composition results in additional defects and strain which degenerate lattice thermal conductivity by reducing its mean free path.

In conclusion, the TE properties of MOCVD grown $\text{In}_x\text{Ga}_{1-x}\text{N}$ were investigated for $x=0.07$ to 0.24. The highest ZT value of alloys was observed as 0.072 for $\text{In}_{0.20}\text{Ga}_{0.80}\text{N}$. This ZT value improvement is enabled by alloy scattering mechanism resulting in high electrical conductivity and low thermal conductivity. In addition, the effect of dislocation density with ZT value of InGaN alloy using HRXRD method was analyzed. The experimental results indicate that InGaN alloys have promising TE properties at room temperature.

This research is supported by National Science Foundation under Faculty Early Career Development Program (CMMI- 1351817). X. W and X. W. would like to thank the support from the National Science Foundation through the University of Minnesota MRSEC under Award Number DMR-1420013.

- ¹ B. C. Sales, *Int J Appl Ceram Tec* **4**(4), 291 (2007).
- ² A. Shakouri, *Annu Rev Mater Res* **41**, 399 (2011).
- ³ E. N. Hurwitz, M. Asghar, A. Melton, B. Kucukgok, L. Q. Su, M. Oroc, M. Jamil, N. Lu, and I. T. Ferguson, *J Electron Mater* **40**(5), 513 (2011).
- ⁴ H. Wang, Z. M. Gibbs, Y. Takagiwa, and G. J. Snyder, *Energ Environ Sci* **7**(2), 804 (2014).
- ⁵ K. Yang, S. Cahangirov, A. Cantarero, A. Rubio, and R. D'Agosta, *Phys Rev B* **89**(12), (2014).
- ⁶ H. H. Xie, H. Wang, Y. Z. Pei, C. G. Fu, X. H. Liu, G. J. Snyder, X. B. Zhao, and T. J. Zhu, *Adv Funct Mater* **23**(41), 5123 (2013).
- ⁷ T. M. Tritt, *Annu Rev Mater Res* **41**, 433 (2011).
- ⁸ A. F. Ioffe, *Sov Phys-Sol State* **1**(10), 1487 (1960).
- ⁹ A. Szein, H. Ohta, J. Sonoda, A. Ramu, J. E. Bowers, S. P. DenBaars, and S. Nakamura, *Appl Phys Express* **2**(11), (2009).
- ¹⁰ S. Yamaguchi, Y. Iwamura, and A. Yamamoto, *Appl Phys Lett* **82**(13), 2065 (2003).

- ¹¹ N. Lu and I. Ferguson, *Semicond Sci Tech* **28**(7), (2013).
- ¹² B. N. Pantha, R. Dahal, J. Li, J. Y. Lin, H. X. Jiang, and G. Pomrenke, *Appl Phys Lett* **92**(4), (2008).
- ¹³ A. Sztejn, H. Ohta, J. E. Bowers, S. P. DenBaars, and S. Nakamura, *J Appl Phys* **110**(12), (2011).
- ¹⁴ A. Sztejn, J. E. Bowers, S. P. DenBaars, and S. Nakamura, *Appl Phys Lett* **104**(4), (2014).
- ¹⁵ W. L. Liu and A. A. Balandin, *J Appl Phys* **97**(7), (2005).
- ¹⁶ A. Sztejn, J. Haberstroh, J. E. Bowers, S. P. DenBaars, and S. Nakamura, *J Appl Phys* **113**(18), (2013).
- ¹⁷ T. Tong, D. Fu, A. X. Levander, W. J. Schaff, B. N. Pantha, N. Lu, B. Liu, I. Ferguson, R. Zhang, J. Y. Lin, H. X. Jiang, J. Wu, and D. G. Cahill, *Appl Phys Lett* **102**(12), (2013).
- ¹⁸ Y. Huang, A. Melton, B. Jampana, M. Jamil, J. H. Ryou, R. D. Dupuis, and I. T. Ferguson, *J Photon Energy* **2** (2012).
- ¹⁹ Y. Huang, A. Melton, B. Jampana, M. Jamil, J. H. Ryou, R. D. Dupuis, and I. T. Ferguson, *J Appl Phys* **110**(6), (2011).
- ²⁰ G. L. Eesley, B. M. Clemens, and C. A. Paddock, *Appl Phys Lett* **50**(12), 717 (1987).
- ²¹ G. T. Hohensee, W. P. Hsieh, M. D. Losego, and D. G. Cahill, *Rev Sci Instrum* **83**(11), (2012).
- ²² D. G. Cahill, *Rev Sci Instrum* **75**(12), 5119 (2004).
- ²³ R. B. Wilson, B. A. Apgar, W. P. Hsieh, L. W. Martin, and D. G. Cahill, *Phys Rev B* **91**(11), (2015).
- ²⁴ F. K. Yam and Z. Hassan, *Superlattice Microst* **43**, 1 (2008).
- ²⁵ M. E. Vickers, M. J. Kappers, T. M. Smeeton, E. J. Thrush, J. S. Barnard, and C. J. Humphreys, *J Appl Phys* **94**(3), 1565 (2003).
- ²⁶ H. Angerer, D. Brunner, F. Freudenberger, O. Ambacher, M. Stutzmann, R. Hopler, T. Metzger, E. Born, G. Dollinger, A. Bergmaier, S. Karsch, and H. J. Korner, *Appl Phys Lett* **71**(11), 1504 (1997).
- ²⁷ M. Schuster, P. O. Gervais, B. Jobst, W. Hosler, R. Averbeck, H. Riechert, A. Iberl, and R. Stommer, *J Phys D Appl Phys* **32**(10A), A56 (1999).
- ²⁸ Hua Tong, Jing Zhang, Guangyu Liu, Juan A. Herbsommer, G. S. Huang, and Nelson Tansu, *Proc. of SPIE* **7939** (2011).
- ²⁹ M. A. Moram and M. E. Vickers, *Rep Prog Phys* **72**(3), (2009).
- ³⁰ R. Singh, D. Doppalapudi, T. D. Moustakas, and L. T. Romano, *Appl Phys Lett* **70**(9), 1089 (1997).
- ³¹ I. K. Park, M. K. Kwon, S. H. Baek, Y. W. Ok, T. Y. Seong, S. J. Park, Y. S. Kim, Y. T. Moon, and D. J. Kim, *Appl Phys Lett* **87**(6), (2005).
- ³² C. A. Parker, J. C. Roberts, S. M. Bedair, M. J. Reed, S. X. Liu, N. A. El-Masry, and L. H. Robins, *Appl Phys Lett* **75**(17), 2566 (1999).
- ³³ D. I. Florescu, V. M. Asnin, F. H. Pollak, R. J. Molnar, and C. E. C. Wood, *J Appl Phys* **88**(6), 3295 (2000).